Synthetic ratio computation for programming population composition and multicellular morphology

Bolin An[1,2,3,#], Tzu-Chieh Tang[4,5,#,*], Qian Zhang[1,#], Teng Wang[1], Kesheng Gan[1], Kun Liu[1], Yuzhu Liu[1], Yanyi Wang[1], William M. Shaw[6,7], Qianyi Liang[1], Yaomin Wang[1], Timothy K. Lu[2,3,8], George M. Church[4,5,*], Chao Zhong[1,*]

[1] Key Laboratory of Quantitative Synthetic Biology, Center for Materials Synthetic Biology, Shenzhen Institute of Synthetic Biology, Shenzhen Institute of Advanced Technology, Chinese Academy of Sciences, Shenzhen, China

[2] Department of Biological Engineering, Massachusetts Institute of Technology, Cambridge, MA, USA

[3] Research Laboratory of Electronics, Massachusetts Institute of Technology, Cambridge, MA, USA

[4] Wyss Institute for Biologically Inspired Engineering, Harvard University, Boston, MA, USA

[5] Department of Genetics, Blavatnik Institute, Harvard Medical School, Boston, MA, USA

[6] Biological Design Center, Boston University, Boston, MA, USA

[7] Department of Biomedical Engineering, Boston University, Boston, MA, USA

[8] Department of Electrical Engineering and Computer Science, Massachusetts Institute of Technology, Cambridge, MA, USA

[#] B.A, T.-C.T and Q.Z. contributed equally

* Correspondence should be addressed to T.-C.T. (zijaytang@gmail.com), G.M.C (gchurch@genetics.med.harvard.edu), and C.Z. (chao.zhong@siat.ac.cn).

ABSTRACT

Recent advancements in genetic engineering have provided diverse tools for artificially synthesizing population diversity in both prokaryotic and eukaryotic systems. However, achieving precise control over the ratios of multiple cell types within a population derived from a single founder remains a significant challenge. In this study, we introduce a suite of recombinase-mediated genetic devices designed to achieve accurate population ratio control, enabling the distribution of distinct functionalities across multiple cell types. We systematically evaluated key parameters influencing recombination efficiency and developed data-driven models to reliably predict binary differentiation outcomes. Using these devices, we implemented parallel and series circuit topologies to create user-defined, complex cell fate branching programs. These branching devices facilitated the autonomous differentiation of precision fermentation consortia from a single founder strain, optimizing cell-type ratios for applications such as pigmentation and cellulose degradation. Beyond biomanufacturing, we engineered multicellular aggregates with genetically encoded morphologies by coordinating self-organization through cell adhesion molecules (CAMs). Our work provides a comprehensive characterization of recombinase-based cell fate branching mechanisms and introduces a novel approach for the bottom-up, high-resolution construction of synthetic consortia and multicellular assemblies.

Main

In multicellular organisms, pattern formation is woven through asymmetric cell divisions, where stem cells give rise to progeny with distinct phenotypes[1, 2]. Through the orchestration of complex gene regulatory networks, eukaryotic stem cells undergo differentiation into specialized cell lineages that integrate seamlessly to form functional tissues or organs. This sophisticated differentiation machinery reflects the genetic intricacy of multicellular eukaryotes and has significantly contributed to their evolutionary triumph[2]. Parallel yet more streamlined phenomena are observed in microorganisms. For example, *Caulobacter crescentus* undergoes asymmetric division to produce motile cells lacking reproductive capabilities and sessile cells capable of division but not motility[3]. Similarly, under nitrogen-limiting conditions, *Anabaena* filaments' central cells asymmetrically divide to generate progeny specialized in nitrogen fixation or photosynthesis, ensuring the survival and proliferation of the colony[4]. Natural selection has consistently favored programmed differentiation and cooperative division of labor, maximizing population fitness. These cellular communities accomplish sophisticated tasks by efficiently allocating resources and exploiting complementary strengths, achieving benefits unattainable by a single cell type[5].

Synthetic biology has unlocked the reprogramming of cellular functions, facilitating the emergence of diverse artificial cell states[6-12], even in simple unicellular systems like *Escherichia coli*. A seminal achievement was the 2000 development of a genetic toggle switch in *E. coli*, enabling reversible switching between two distinct states[13]. Advances in genetic tools have since enabled engineered bacterial stem cells through mechanisms such as the bacterial chromosome partitioning system (par), inducing asymmetric cell division, and generating progeny with distinct genetic content[7]. Epigenetic tools, including phase-separated and scaffolding proteins like PopZ, have further advanced microbial cell differentiation[8, 9]. Beyond bacteria, mammalian systems have also been engineered; for example, the MultiFate circuit generates multiple cellular phenotypes in Chinese hamster ovary (CHO) cells[14]. These examples highlight the potential of genetic circuits to program and rewrite cell fate. However, scaling genetic toggle switches and DNA partitioning systems with increasing cell states and quantitatively controlling the ratio of specific cell types within offspring populations remain challenges. Moreover, most artificial systems are incapable of autonomously generating complex multicellular systems from a single founder cell type. These limitations impede the capacity of synthetic communities to differentiate autonomously and accurately perform complex tasks, thereby constraining their potential in biomanufacturing, regenerative medicine, and therapeutic applications.

Recombinases, enzymes that catalyze recombination between specific DNA sequences, offer a promising solution. These enzymes target *attB* (bacterial) and *attP* (phage) sites, with recombination outcome—excision or inversion— determined by the number and orientation of these sites[15]. Serine recombinases, favored for their irreversible actions and independence from additional cofactors, are widely used in constructing Boolean logic gates[16], amplification circuits[17], and information storage systems[18, 19]. Strategic positioning of multiple *att* sites enables programmable rearrangement of gene elements, expanding the toolbox for cell state programming[18, 20].

Here, we present a suite of recombinase-based cell fate branching devices for generating diverse progeny cell types with user-defined ratios and quantitatively managing multicellular morphology. This technology enables precise ratio control within synthetic communities, where differentiated cells arise from a single founder cell type. By manipulating DNA sequences between *att* sites and employing mutated *att* variants, we achieved high-precision control over the ratios (0.1%-99.9%) of two progeny cell types bifurcated from a single founder. Our branching devices can be implemented in parallel or series configurations, enabling scalability and complex outputs, including transcription factors, secreted enzymes, and biosynthesis pathways. Additionally, we used cell surface display and synthetic adhesion molecules to engineer self-organizing cellular architectures with highly controllable geometries differentiated from a single founder. This platform offers a versatile approach for quantitatively controlling cell differentiation behavior across species, with applications ranging from organoid design to multitasking microbial communities for precision fermentation and bioremediation.

Results

Design and characterization of cell fate branching devices

Binary cell fate branching devices were developed using a Bxb1 recombinase-based framework. The device contained a single Bxb1 *attP* site flanked by two identical Bxb1 *attB* sites in the configuration *attB-attP-attB* (**Fig. 1a**). Recombination between the *attP* site and one of the *attB* sites was triggered by the recombinase, resulting in the excision of either the left or right DNA segment and the generation of two distinct recombination products (**Fig. S1**). To ensure the differentiation of each parent cell into a single progeny type, the system was constructed to allow only one copy of the device per genome. We assumed that such a mechanism would be host-agnostic and set out to test our hypotheses in model bacterial (*E. coli*), yeast (*Saccharomyces cerevisiae*), and mammalian (HEK293) systems.

To track differentiation, two constitutive promoters with comparable transcription strengths were incorporated into the branching device. The promoters were arranged to face opposite directions and separated by *att* sites, creating a genetic device in the order *attB-attP-attB* (**Fig. 1a**). We also placed terminators between the promoters and the outputs to prevent leaky expression. Reporter genes encoding Venus (green fluorescence) and mScarlet (red fluorescence) were positioned on opposite sides. Fluorescent reporter expression was repressed until the expression of the Bxb1 recombinase was induced by small molecules, such as aTc or β-estradiol (**Fig. S2**). Following induction, recombinase-mediated DNA excision allowed for the activation of either Venus or mScarlet expression. Flow cytometry and confocal fluorescence microscopy were used to confirm the differentiation of founder cells into two distinct populations that exhibited either green or red fluorescence, with no overlap observed across three diverse hosts (**Fig. 1b-d**, **Fig. S3**).

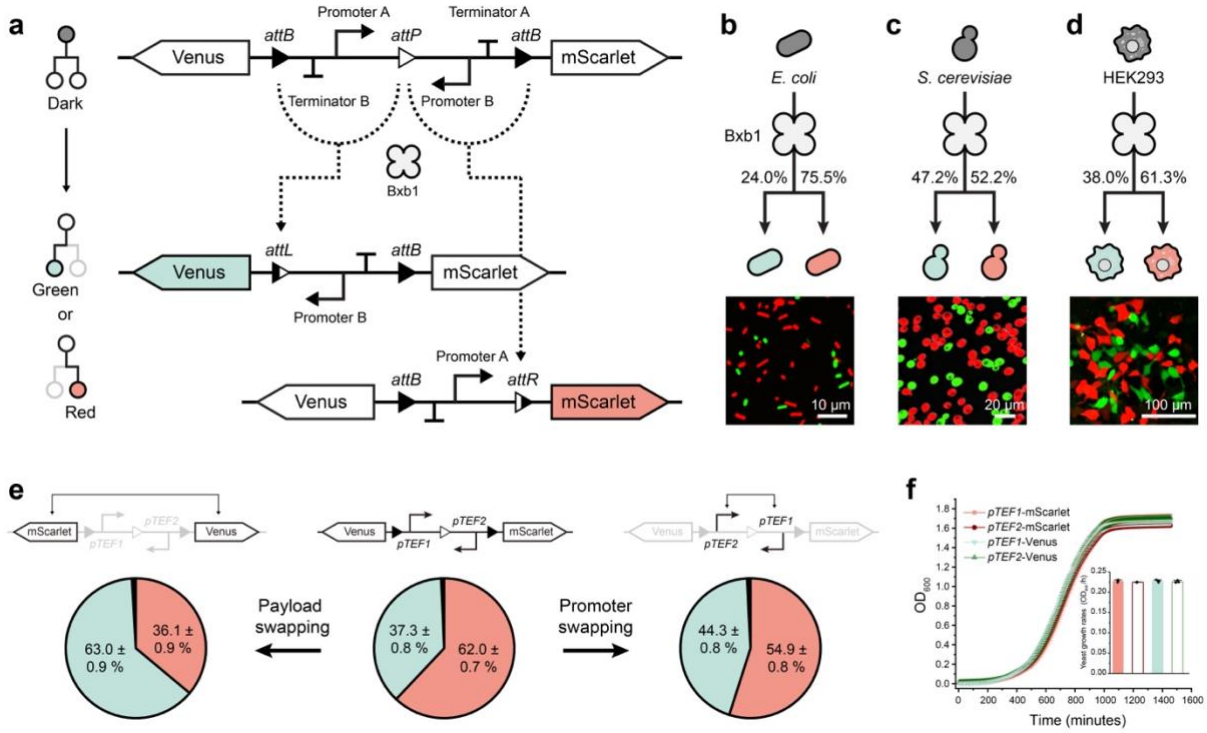

Fig. 1 | **Design and characterization of gene devices for cellular differentiation control. a**, Diagram illustrating the design of general branching devices that probabilistically generate two types of fluorescent cells. **b-d**, Schematics and fluorescence data demonstrating cellular differentiation in engineered cells: *E. coli* (**b**), *S. cerevisiae* (**c**), and HEK293 cells (**d**). Progeny cell type ratios were determined via flow cytometry and confocal fluorescence microscopy analysis (*n* = 3 independent experiments). **e**, Factors influencing yeast cellular differentiation driven by the designed gene devices. Progeny cell ratios were measured by flow cytometry (*n* = 3 independent experiments, mean ± SD). **f**, Growth curves of four selected yeast strains, with their respective growth rates shown in the inset for comparison (*n* = 4 independent experiments, mean ± SD).

To systematically investigate the branching mechanism, we use the model unicellular eukaryote *S. cerevisiae* as the chassis for detailed characterization, owing to its extensive genetic tools and highly efficient homologous recombination that expedites rapid, iterative genome engineering. We swapped the two fluorescent reporters and promoters within the genetic circuit to probe the underlying factors leading to the observed constant progeny cell ratios. Notably, in *S. cerevisiae*, when fluorescent proteins are used as reporters, we found that terminators between the *att* sites are not required to prevent leaky expression of the output (**Fig. S4-S5**). Therefore, to simplify the design, the branching devices in the following investigation only separate the promoter and coding sequence of fluorescent proteins with another promoter in the reverse complement strand to inhibit output gene expression.

As depicted in **Fig. 1e**, swapping the two fluorescent reporters did not appreciably change the outcome of the recombination event. Progeny with the reporter on the left side consistently represented 36.1 ± 0.9% and 37.3 ± 0.8% of the population in the two designs (**Fig. 1e**). However, swapping the positions of the promoters led to altered ratios, with green cells increasing from 37.3 ± 0.8% to 44.3 ± 0.8% and red cells decreasing from 62.0 ± 0.7% to 55.9 ± 0.8% (**Fig. 1e**). We conducted a growth rate analysis

of the four yeast progenies (labeled *pTEF1*-mScarlet, *pTEF2*-mScarlet, *pTEF1*-Venus, and *pTEF2*-Venus, according to their respective promoter-reporter pairings) differentiated from the branching devices shown in **Fig. 1e** and found they share indistinguishable growth rates (0.22~0.23 OD_{600}/hour, **Fig. 1f)**. Furthermore, competition assays based on passaging every 24 hours at 1000-fold dilution for seven days show that the red-to-green ratio remains essentially constant (**Fig. S6**). These findings collectively suggest that the observed variation in progeny ratio is not a consequence of differential growth caused by metabolic burden associated with protein overexpression but rather the result of recombinase action on different device topologies.

Exploration of critical factors influencing cell differentiation devices

Sequence between att sites and steric hindrance

We hypothesized that promoter strength could influence differential excision and tested this by systematically varying promoters positioned between *att* sites. Ten promoters, ranging from the strongest (*pTDH3*) to the weakest (*pREV1*), were incorporated into the left and right arms of our branching device design (**Fig. 2a, Fig. S7**). A library of 90 unique designs, combining these promoters, revealed distinct progeny cell ratios upon recombinase induction (**Fig. 2b, Fig. S8-S17**). For example, a device with *pTDH3* on the left arm and *pREV1* on the right arm resulted in 84.5 ± 1.0% red fluorescent cells (**Fig. S15a**). In contrast, a device featuring *pTEF2* and *pRPL18B* yielded only 15.0 ± 1.3% red fluorescent cells (**Fig. S17d**). Growth assays indicated no significant metabolic burden from expressing fluorescent proteins driven by strong or weak promoters over a week of competition (**Fig. S18-S19**). The closer analysis demonstrated that strong promoters, such as *pTDH3*, reduced Bxb1 recombination efficiency when located between *att* sites (**Fig. 2b**). For instance, devices with *pTDH3* on the left arm and *pREV1* on the right arm showed only 14.9 ± 1.0% green fluorescent cells, suggesting a bias toward right-arm excision (**Fig. S15a**). Substituting *pTDH3* with the weaker *pSAC6* promoter increased the proportion of green cells to 60.9 ± 0.7%, favoring left-arm excision (**Fig. S14a**). We propose that steric hindrance from transcription machinery recruited by strong promoters may obstruct recombinase binding and DNA bending, reducing recombination efficiency.

To investigate steric hindrance further, we inserted Tet operator (*TetO*) sequences, specific binding sites for the tetracycline repressor (TetR), between *att* sites in *attB-attP* or *attP-attB* configurations (**Fig. S20a-b**). Next-generation sequencing (NGS) revealed that TetR binding decreased recombination efficiency, with the rate for *attB-attP* sites dropping from 61.0 ± 4.3% in the absence of TetR to 39.1% in its presence (**Fig. S20a**). Similar results were obtained with dCas9 and guide RNA targeting sequences between *att* sites (**Fig. S20c**). These findings indicate that steric constraints imposed by sequences between *att* sites significantly affect recombination efficiency across various yeast promoters (**Fig. 2a**). Additionally, replacing promoters with 100 bp non-functional random DNA sequences of varying GC content revealed substantial variations in recombination frequencies, independent of GC content (**Fig. S21**). These results suggest the involvement of other unknown factors

influencing Bxb1 recombination. As functional promoters are necessary for gene expression outputs, subsequent investigations focused on branching devices with one promoter on each arm.

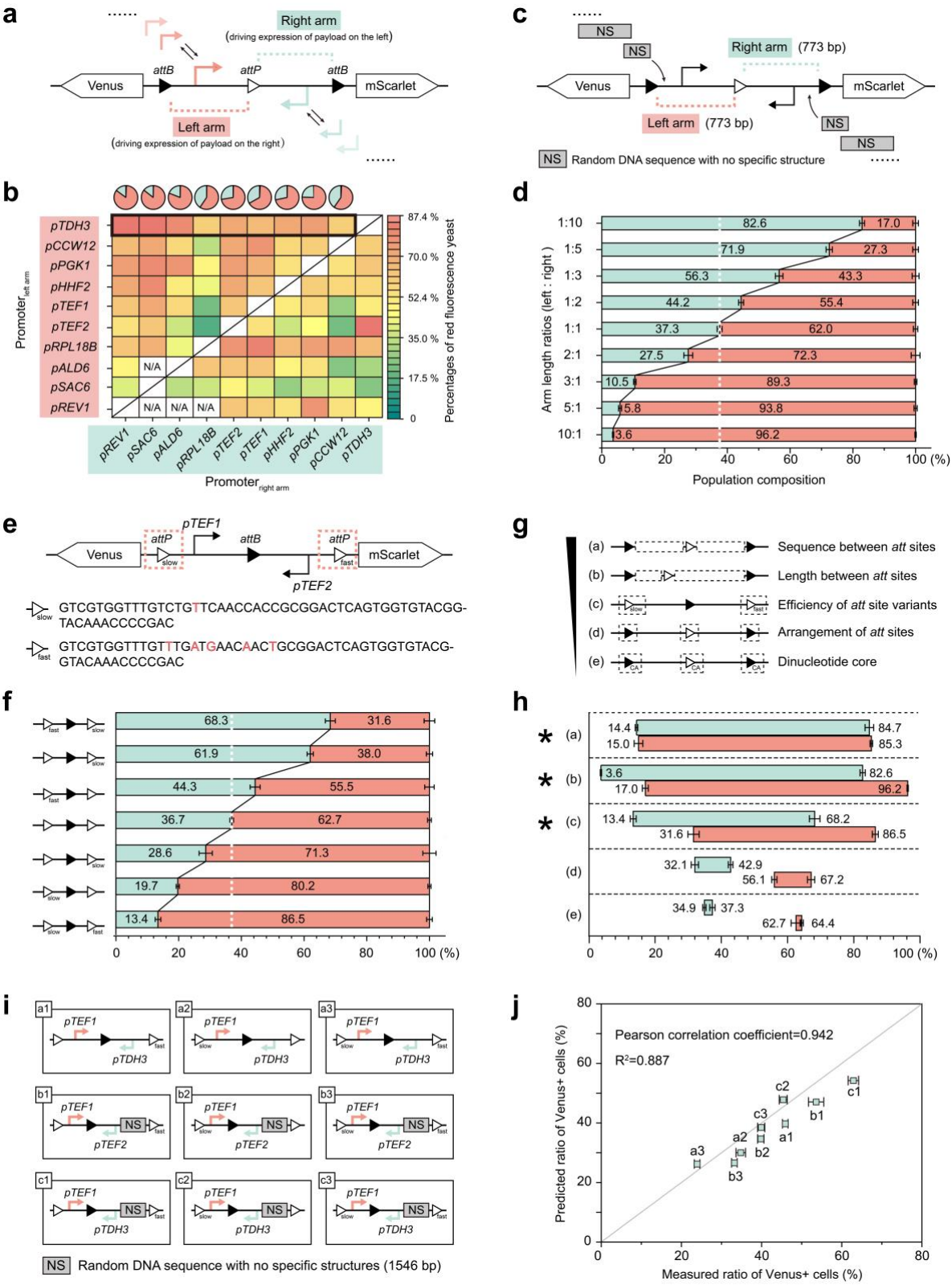

Fig. 2 | Identifying factors influencing the performance of recombinase-based cellular differentiation circuits. a, Schematic of branching devices using different yeast promoters placed on the left or right arm. **b**, Heat map comparing the performance of 90 constructed strains, each with two different constitutive yeast promoters on the arms. The transcriptional strength of the promoters decreases from the strongest *pTDH3* to the weakest *pREV1*. Red intensity indicates the percentage of red fluorescence cells. The pie chart above shows the statistics of progeny cells for the representative data points marked by the thick black borders. "N/A" denotes circuits where progeny proportions could not be quantified via flow cytometry (n = 3 independent experiments, mean ± SD). **c**, Branching device design with added nonsense (NS) DNA sequences to adjust promoter arm lengths. **d**, Flow cytometry data showing differentiated cell distributions for circuits with left-to-right arm length ratios ranging from 1:10 to 10:1 (n = 3 independent experiments, mean ± SD). **e**, Schematic of cell fate branching device design using two *attP* site mutants with different recombination efficiencies. Mutated bases in $attP_{slow}$ and $attP_{fast}$ are shown in red. **f,** Flow cytometry data showing branched cell distributions for seven circuits with different *attP* mutants (n = 3 independent experiments, mean ± SD). **g**, Summary of five factors influencing the output cell differentiation devices. **h**, Comparison of progeny cell differentiation ratios from circuits incorporating each of the 5 selected factors, showing that the first three factors significantly expand progeny cell distributions. **i**, Nine representative circuit designs used for mathematical model predictions. **j**, Comparison between model-predicted Venus cell ratios and flow cytometry data from designs in **Figure 2i**.

Length of promoter arms between att sites

We next evaluated how the length of promoter-containing DNA sequence between *att* sites impacts recombination efficiency (**Fig. 2c**). We hypothesized that increasing DNA length would decrease recombinase tetramerization likelihood, influencing branching outcomes. By varying the length of DNA on one arm while maintaining a fixed length on the other, we observed a consistent impact on progeny cell proportions (**Fig. 2d**). Increasing the length of the right arm relative to the left (1:1 to 1:10) reduced the proportion of red fluorescent cells from 62.0 ± 0.7% to 17.0 ± 0.9% (**Fig. 2d, Fig. S22**). Conversely, elongating the left arm (1:1 to 10:1) increased red fluorescent cells to 96.2 ± 0.2% (**Fig. 2d, Fig. S23**). Fixed-length, nonfunctional DNA sequences showed relatively mild effects compared to DNA length differences (**Fig. S24**). These results confirm that DNA sequence length flanked by *att* sites modulates recombinase efficiency and progeny cell distribution.

att site mutants and recombination efficiency

Variants of Bxb1 *att* sites can directly impact the recognition and binding of the Bxb1 recombinase to the DNA molecule[21]. By exploiting the differential affinities of recombinases to distinct *att* sites with varying recombination kinetics, we hoped to selectively modulate the enzyme's catalytic preference within branching devices, thus enabling tuning of sub-population ratios (as depicted in **Fig. 2e**). Our study employed an $attP_{slow}$ variant, which contains a C14A mutation, and $attP_{fast}$, featuring multiple substitutions (5A, 8T, 12C, 14T, and 17A) (**Fig. 2e**). Since $attP_{slow}$ demonstrates reduced recombination efficiency compared to the more efficiently processed $attP_{fast}$, we designed six distinct branching device configurations by enlisting wild-type and variant *att* sites to modulate recombination preferences (**Fig. 2f**, **Fig. S25**). The results verified that the configuration of *attP* variants significantly influenced progeny cell fluorescence ratios. For instance, the $attP_{fast}$-*attB*-$attP_{slow}$ arrangement yielded 68.3 ± 1.6% green fluorescent cells, while the $attP_{fast}$-*attB*-*attP* configuration resulted in 44.3 ± 1.6%. The $attP_{slow}$-*attB*-$attP_{fast}$ setup produced 13.4 ± 0.9% green fluorescent cells (**Fig. 2f, Fig. S25**). These findings

demonstrate the potential for *att* site variants to selectively program recombinase-based cell differentiation outcomes.

Minor factors influencing the output of branching devices

Arrangement of att sites in the branching device

The general architecture of our branching devices included three *att* sites (**Fig. 1a**), resulting in 16 possible permutations of *att* type (*attB* or *attP*) and orientation (**Fig. S26**). Each configuration was tested in yeast (**Fig. S26-S28**), and all designs, including the prototype in **Fig. 1a**, consistently generated two distinct progeny cell types with minor variations in ratios, generally not exceeding 10% (**Fig. S26**). The proportion of green fluorescent cells fluctuated between 32.1 ± 1.1% and 42.9 ± 0.7% across all configurations. These results suggest that the specific arrangement and orientation of *att* sites only mildly impact recombination and differentiation outcomes. Notably, Bxb1-mediated DNA inversion was preferred over DNA excision events when both competed against each other (**Fig. S26b**).

Orthogonal dinucleotides in att sites

The central dinucleotide of *att* sites generates a 2-bp overhang that mediates ligation between cleaved *attB* and *attP* sites with complementary overhangs[22]. While all devices in this study used the GA dinucleotide[23], six alternative dinucleotides (GT, TT, CA, CC, CT, and TC as control) were tested to assess their potential effects (**Fig. S29**). Each variant recombined exclusively with *att* sites containing complementary dinucleotides, allowing up to six independent recombination events with a single recombinase. However, when these dinucleotides were applied in the *attB-attP-attB* branching device, the distribution of red and green fluorescent cell populations remained consistent. For instance, the green fluorescent cell fraction ranged from 34.9 ± 0.5% and 37.3 ± 0.8% (**Fig. S29**-**S30**). These findings indicate that orthogonal *att* variants do not appreciably alter cell state ratios, supporting the integration of multiple orthogonal devices within a single genome to enable complex circuit designs.

Differential cell growth rates

To examine the impact of protein payloads and differential cell growth rates on progeny cell ratios, the Venus reporter was replaced with several recombinases (e.g., No67[24], TP901[25], R4[25], PhiC31[25]) and synthetic transcription factors (e.g., SrpR-VP16[26], Bm3R1-VP16[26]). These replacements were incorporated into branching devices designed to produce a 1:1 ratio of Venus- to mScarlet-expressing cells, with full differentiation achieved after 8 hours (**Fig. S31**). Following an 18-hour induction period, limited variation in progeny cell-type distribution was observed with R4 recombinase, resulting in 51.8 ± 0.6% R4-expressing and 48.2 ± 0.6% mScarlet-expressing progeny cells (**Fig. S31-S33**). Conversely, devices containing No67 and mScarlet exhibited an increase in red fluorescent cells from 52.3% at 8 hours to 57.6% at 18 hours, suggesting minor toxicity of the No67 recombinase (**Fig. S34**). This effect

was more pronounced with PhiC31 recombinase, where red fluorescent cells increased from 57.9% at 8 hours to 94.3% at 18 hours (**Fig. S35**). These observations highlight the potential to utilize differential growth rates to dynamically modulate progeny cell ratios over time (**Fig. S36**).

Choice of recombinases

To evaluate the generality of these observations with Bxb1-based devices, additional serine recombinases (e.g., TP901, R4, A118) were tested (**Fig. S37**). Flow cytometry analysis confirmed that all serine recombinases tested effectively induced differentiation, generating progeny cells in two distinct states. However, significant disparities in progeny cell distributions were noted. For instance, the TP901-based system produced approximately 16.5 ± 0.2% green fluorescent cells and 79.4 ± 0.6% red fluorescent cells, with the remainder showing no fluorescence (**Fig. S37**). By contrast, the A118-based system yielded approximately 38% green, 39% red, and 23% undifferentiated cells (**Fig. S37**). When undifferentiated cells from the A118-based system were re-induced in fresh YPD medium, a similar differentiation pattern re-emerged: 38% green, 39% red, and 23% undifferentiated cells (**Fig. S38**). Similarly, partially induced Bxb1-based systems displayed repeatable differentiation patterns (**Fig. S38**). These results indicate that potential construct asymmetric differentiation systems where specific founder cell ratios retain pluripotency, thereby prolonging system stemness.

Developing a computational model for predicting cell differentiation outcomes

Our exploration of factors influencing cell differentiation emphasized the significance of functional DNA elements between *att* sites, the length of intervening DNA sequences, and the recombination efficiencies of *att* site variants **(Fig. 2g-h**). These factors were systematically incorporated into a computational model designed to predict differentiation outcomes in engineered branching devices (**Fig. S39-S40, Table. S1-S3**). Using data from nine distinct genetic devices, the model exhibited strong predictive power, accurately reflecting observed differentiation behaviors **(Fig. 2i-j, Fig. S41)**. Integrating additional minor factors, such as differential growth rates, could further enhance predictive precision.

Precise ratio multiplication through parallel genetic devices

Parallel branching devices were designed to function orthogonally within a genome. Each device undergoes independent Bxb1-mediated recombination, producing progeny cells with distinct traits. The probability of generating each cell type is determined by multiplying the probabilities of individual states in the branching devices. For n devices, this approach yields 2^n unique cell types, each defined by specific trait combinations (**Fig. S42**). For example, with two devices producing outputs for green and red fluorescence, the probability of a progeny cell being yellow (expressing both green and red fluorescence) is calculated as:

$$P(green \cap red) = P(green) \cdot P(red)$$

To validate the rule of multiplication, we integrated two orthogonal branching circuits into the yeast genomes: one using ShadowG and Venus, and another using ShadowG and mScarlet (**Fig. 3a**). Following Bxb1 induction, four progeny cell types emerged, corresponding to distinct fluorescence states: dark (no fluorescence), green, red, and yellow (both green and red fluorescence, **Fig. 3b**). Utilizing the probabilities measured from strains hosting only one of the two branching devices (**Fig. S43-S45**), we computed the theoretical distribution of the four progeny cell types in the final mixed population (**Fig. 3b**). Flow cytometry confirmed a strong correlation between the predicted probabilities and the observed cell type proportions (**Fig. 3c**). We also inoculated ~1000 founder cells on an agar plate supplemented with the inducer and observed colonies with four-color stripes under fluorescence microscopy (**Fig. 3d**). Varying individual branching device designs yielded results reflecting the modified ratios, with the theoretical progeny cell distribution closely resembling the experimental outcomes, highlighting the robustness of the rule of multiplication (**Fig. S46-S57**).

Expanding the system to three orthogonal branching devices (**Fig. 3e**) yielded eight progeny types. For instance, the probability of generating white cells expressing all three fluorescent proteins (green, red, and blue) was computed as:

$$P(green \cap red \cap blue) = P(green) \cdot P(red) \cdot P(blue)$$

Both fluorescence microscopy and flow cytometry confirmed that the experimental distributions of eight progeny cell types matched their theoretical predictions (**Fig. 3f-g**, **Fig. S58**). Fluorescence microscopy further demonstrated all eight fluorescent states in both liquid and solid media (**Fig. 3h**). By modifying branching device parameters, various cell-type distribution ratios were achieved (**Fig. S59-S62**). In all configurations, theoretical distributions aligned closely with experimental findings, confirming the robustness of the rule of multiplication and its broad applicability.

Stacking parallel branching devices to achieve extreme ratios

Thus far, the lowest ratio achieved with a single branching device was 3.6%, modulated by arm length (**Fig. 2d**). Given that parallel branching devices enable robust multiplication computation, we hypothesize one can achieve <3.6% during cell differentiation using the previously demonstrated rule of multiplication. By deploying analogous branching devices in parallel within a single founder strain, we implemented exponential functions to generate progeny populations with extremely low ratios.

We designed a branching device utilizing the transcriptional repressor LacI. In this system, LacI expression occurs ~91.6% of the time post-differentiation. When mScarlet was placed under the control of *pLac* promoter (which activates only in the absence of the LacI repressor), the probability of progeny cells expressing red fluorescence was calculated as:

$$P(red) = 1-P(LacI)$$

Experimentally, this yielded ~8.4% red fluorescent progeny, validating the model (**Fig. 3i, Fig. S63a-c**).

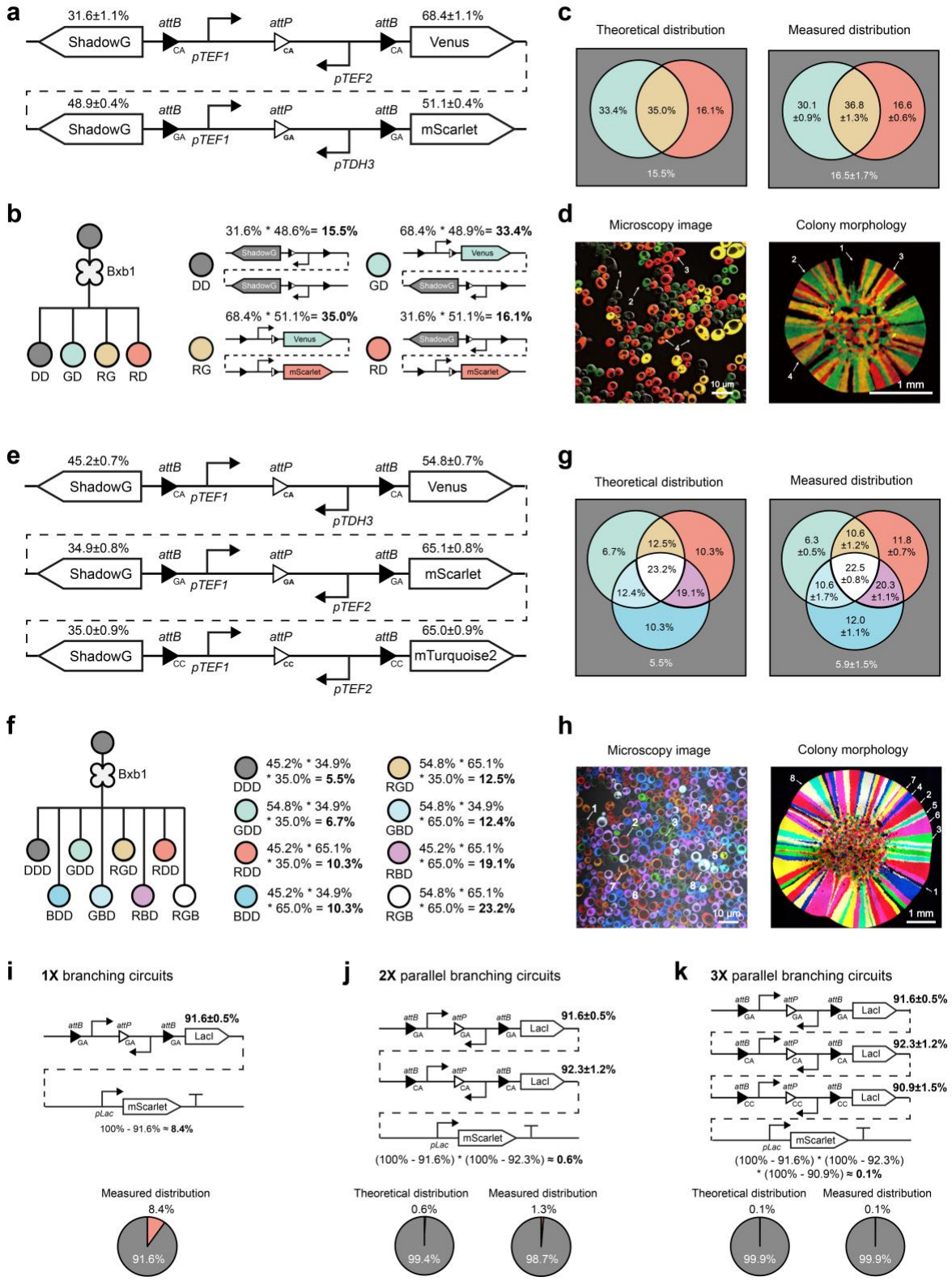

Fig. 3 | **Designing parallel orthogonal genetic circuits for quantitatively controlled cell states. a,** Schematic of a 2x orthogonal branching circuit design. The first circuit uses CA *att* sites with *pTEF1* and *pTEF2* promoters, and ShadowG and Venus as reporters. The second circuit uses GA *att* sites with *pTEF1* and *pTDH3* promoters, and ShadowG and mScarlet as reporters. Progeny proportions represent the probability of reporter expression. **b**, Theoretical progeny types and proportions from the 2× orthogonal circuit: **DD** (ShadowG only, non-fluorescent), **GD** (Venus + ShadowG, green fluorescence), **RG** (mScarlet + Venus, red and green fluorescence), **and RD**

(mScarlet + ShadowG, red fluorescence). **c**, Comparison of theoretical progeny distributions with flow cytometry results (*n* = 3 independent experiments, mean ± SD). **d**, Fluorescence microscopy images showing four distinct cell populations in solution (left) and colonies (right). **e**, Schematic of a 3× orthogonal branching circuit. **f**, Theoretical progeny types and proportions from the 3× orthogonal circuit. **g**, Comparison of theoretical distributions with flow cytometry data (*n* = 3 independent experiments, mean ± SD). **h**, Fluorescence microscopy images showing eight distinct cell populations in solution (left) and colonies (right). **i**, Schematic design and flow cytometry data of a 1x cell branching circuit. **j**, Schematic design, theoretical distribution, and flow cytometry data for a 2x parallel cell branching circuit. **k**, Schematic design, theoretical distribution, and flow cytometry data for a 3x parallel cell branching circuit.

When two orthogonal repressor-based branching devices were integrated into the same genome, the probability of progeny cells with no inhibiting mScarlet expression was:

$$P(red) = [1-P(LacI)]^2$$

This computation predicted a 1% red fluorescent progeny ratio, confirmed experimentally (**Fig. 3j, Fig. S63d)**. Adding a third analogous device further reduced the likelihood of red fluorescent progeny to:

$$P(red) = [1-P(LacI)]^3 = 0.1\%$$

This prediction also matched experimental results (**Fig. 3k, Fig. S63e**).

We envision this “exponential function” can be easily expanded by installing up to six analogous, orthogonal Bxb1-based branching devices with different dinucleotides across various chromosomes to avoid homology-induced looping out, achieving rations in the 10^{-6} range. Notably, replacing the LacI repressor with the reverse tetracycline transactivator rtTA also enables comparable exponential operations (**Fig. S64**), indicating the universality of such designs. The ability to quantitatively program the probability of rare events, as demonstrated here, has potential applications in pattern formation or developmental processes where extra-low ratios of specific cell types are required to trigger the establishment of morphogen gradients[27].

Branching devices in series for programming sequential differentiation

Multicellular organism development is a hierarchical process in which development involves stem cells undergoing sequential differentiation into specialized progeny, guided by external cues that enable adaptation to environmental conditions. To replicate this process, we engineered branching devices that allow cells to differentiate sequentially into predefined populations in response to specific signals. These devices use cascading recombinase-based circuits, each inducible by small molecules, to program sequential cellular functions.

Fig. 4a and **Fig. 4b** illustrate our design, featuring two branching devices in series activated by distinct recombinases, Bxb1 and TP901. To prevent leaky expression and ensure optimal performance, terminators were placed between *att* sites (**Fig. S65**). The first branching device uses β-estradiol-inducible Bxb1 to direct founder cells into two progeny types: those constitutively expressing mTurquoise2 (blue) and those retaining an inducible TP901 cassette (dark). TP901 subsequently governs the differentiation of dark cells into green or red fluorescent cells upon aTc induction.

In the presence of β-estradiol alone, 52.7% of the progeny remained dark, while 47.3% fully differentiated into blue cells (**Fig. 4c, left**). Dark progenitors retained multipotency, differentiating into green and red cells only after aTc induction (**Fig. 4c, right**). The final proportions of green and red cells were determined by multiplying the ratio of dark cells at the first layer by their respective differentiation ratios at the second layer:

$$P(green)_{terminal} = P(TP901)_{layer\ 1} \cdot P(green)_{layer\ 2}$$

$$P(red)_{terminal} = P(TP901)_{layer\ 1} \cdot P(red)_{layer\ 2}$$

The calculated ratios, 16.9% green and 34.8% red, closely matched the experimental results (**Fig. 4d, Fig. S66-S67**). Minor discrepancies in the dark cell population were attributed to incomplete differentiation, leaving residual stem cells. This validated system enabled the engineering of a founder strain capable of stepwise differentiation into three cell types secreting laccase, Mel1, and lipase, forming a yeast consortium effective at degrading water contaminants (**Fig. S68**). Furthermore, transcription factors were shown to function with these devices, facilitating the sequential execution of genetic programs with multiple transcriptional units (**Fig. S69**).

We evaluated the scalability of these designs in both horizontal (output diversity) and vertical (circuit depth) expansions. A two-layer binary branching circuit was constructed, resulting in four cell types upon full differentiation (**Fig. 4e, Fig. S70**). The first branching device, activated by β-estradiol-inducible Bxb1, generated two intermediate progenitor types. One type expressed A118, directing differentiation into dark (ShadowG) or blue (mTurquoise2) cells via second branching devices. The other type expressed TP901 in the presence of aTc, driving differentiation into green (Venus) and red (mScarlet) cells (**Fig. 4f-h**). Although recombination inefficiencies in TP901 and A118 led to an increased number of dark cells, the observed distributions aligned with predictions (**Fig. 4h**).

To mitigate inefficiency propagation in deeper circuits, we incorporated the highly efficient Cre recombinase into a three-layer series design (**Fig. 4i**). Each layer contained one branching device responsive to sequential inputs (β-estradiol → aTc → β-estradiol), producing four terminal cell types (**Fig. 4j, Fig. S71**). The ratio of red cells in the final cell population was defined as:

$$P(red)_{terminal} = P(Bxb1)_{layer\ 1} \cdot P(TP901)_{layer\ 2} \cdot P(red)_{layer\ 3}$$

Fig. 4k and **Fig. 4l** show that replacing A118 with Cre greatly reduced recombination inefficiencies. No observable leakiness occurred across layers, and reusing β-estradiol as an input greatly expands the versatility of this series design under a limited number of inducer species.

In summary, we demonstrated that sequential differentiation through branching devices arranged in series provides high programmability and control, akin to natural morphogen-driven processes. This platform offers a robust framework for implementing complex genetic circuits with applications in synthetic biology and cellular engineering.

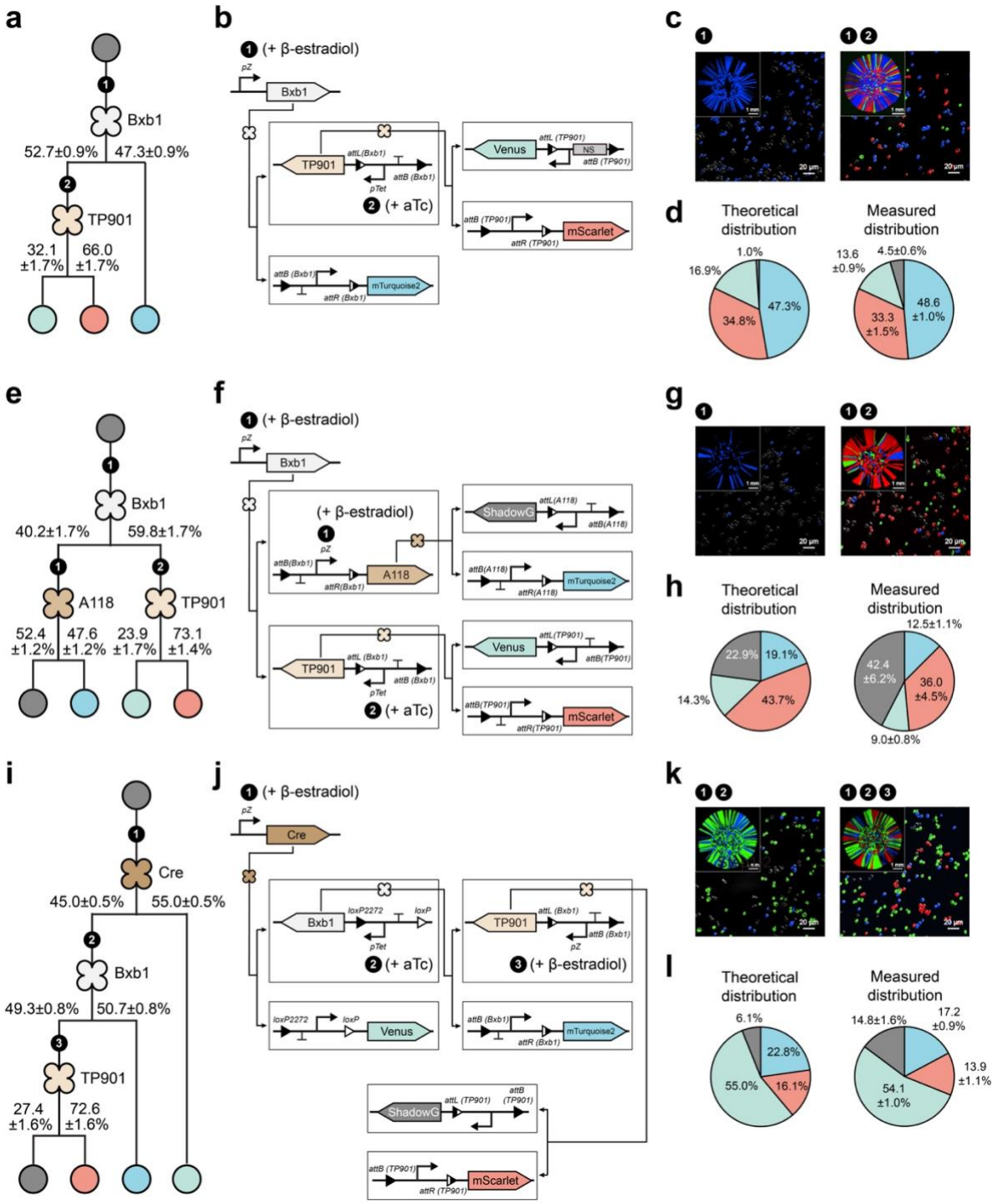

Fig. 4 | Sequential genetic circuits for controlled creation of diverse cell states. a, Schematic of a 2-layer branching device using 2 recombinases to sequentially differentiate cells into 3 terminal cell types. Experimentally determined progeny proportions were used to calculate expected circuit outputs. **b**, Circuit changes during 2-step sequential differentiation. **c**, Fluorescence microscopy images displaying cell population changes at each step. **d**, Comparison of theoretical progeny distributions with flow cytometry data (n = 3 independent experiments, mean ± SD). **e**, Schematic of a 2-layer branching device using 3 recombinases to produce 4 progeny types. **f**, Circuit changes during 2-step differentiation. **g**, Fluorescence microscopy images displaying cell population changes at each step. **h**, Comparison of theoretical distributions with flow cytometry data (n = 3 independent experiments, mean ± SD). **i**, Schematic of a 3-layer branching device using 3 recombinases to differentiate into 4 progeny types. **j**, Circuit changes during 3-step sequential differentiation. **k**, Fluorescence microscopy images displaying cell

population changes at each step. **I**, Comparison of theoretical distributions with flow cytometry data (*n* = 3 independent experiments, mean ± SD).

From a single strain to a consortium of synergistic members

Using branching devices in various circuit layouts, we have demonstrated inducible cellular differentiation programs that generate multiple cell types in tunable ratios from a single founder strain. This approach not only expands microbial system functionality but also facilitates synergistic interactions among differentiated cell types, thereby improving consortium performance. Importantly, this strategy goes beyond simple co-cultures to focus on cases where specific cell-type ratios play a key role in modulating the macroscale population phenotype. To illustrate this, two multi-gene biosynthetic pathways were selected to produce pigments: violacein and β-carotene. Violacein, a purple bis-indole pigment, is synthesized by five enzymes: VioA, VioB, VioC, VioD, and VioE[28] (**Fig. 5a**). β-carotene, a vibrant orange pigment, is produced by four enzymes: CrtI, CrtE, CrtYB, and tHGM1[28] (**Fig. 5a**). By fine-tuning the ratios of the two cell types synthesizing these pigments, a spectrum of colors was created by blending these colors.

To control these pathways, two synthetic transcription factors, Z_3EV and PhIF-VP16, were used to regulate violacein and β-carotene biosynthesis, respectively (**Fig. 5b, Fig. S72a**). A single branching device differentiated the founder strain into two specialized strains: one using Z_3EV to drive violacein production and the other using PhIF-VP16 to trigger β-carotene biosynthesis. Adjusting the proportions of these two “pixel” cell types resulted in cultures that displayed colors ranging from pure purple to pure orange, with four intermediate colors (**Fig. 5c**). Extracted dyes showed absorbance profiles matching their genetically encoded pigments (**Fig. 5d, Fig. S72b**). This “genetic color palette” approach reduces metabolic stress on individual cells through the division of labor and demonstrates its potential for designing self-pigmenting living materials[29].

Branching devices were also applied to cooperative enzymatic reactions relevant to industry. A cellulose-degrading system was chosen as a model, involving three cellulases—EG2, CBH2, and BGL1[30], each performing a step in breaking down cellulose into glucose (**Fig. 5e**). These enzymes were integrated into a two-layer sequential genetic circuit controlled by recombinases Bxb1 and TP901, directing the founder strain to differentiate into three distinct cellulase-secreting progeny cell types (**Fig. 5f**). The performance of these engineered consortia was evaluated by measuring glucose production from engineered yeast supernatants degrading Avicel-101 using the DNS method[31] (**Fig. S73**). Two consortia with different cellulase-secreting cell ratios were tested: Consortium A (BGL1: EG2: CBH2 at 2:3:5) and Consortium B (5:2:3). Both consortia produced significantly more glucose than strains secreting only one cellulase (**Fig. 5g**). Consortium A, with optimized enzyme ratios, outperformed the control strain, producing equal amounts of each cellulase (1:1:1) while maintaining faster growth rates (**Fig. S74**). These results highlight how fine-tuning cell-type ratios can enhance consortium efficiency. The universality of branching devices across different genetic systems makes them a powerful tool for engineering functionally diverse consortia. These consortia, derived from a single founder strain, can

perform complex tasks and processes, offering new possibilities for synthetic biology and industrial biotechnology.

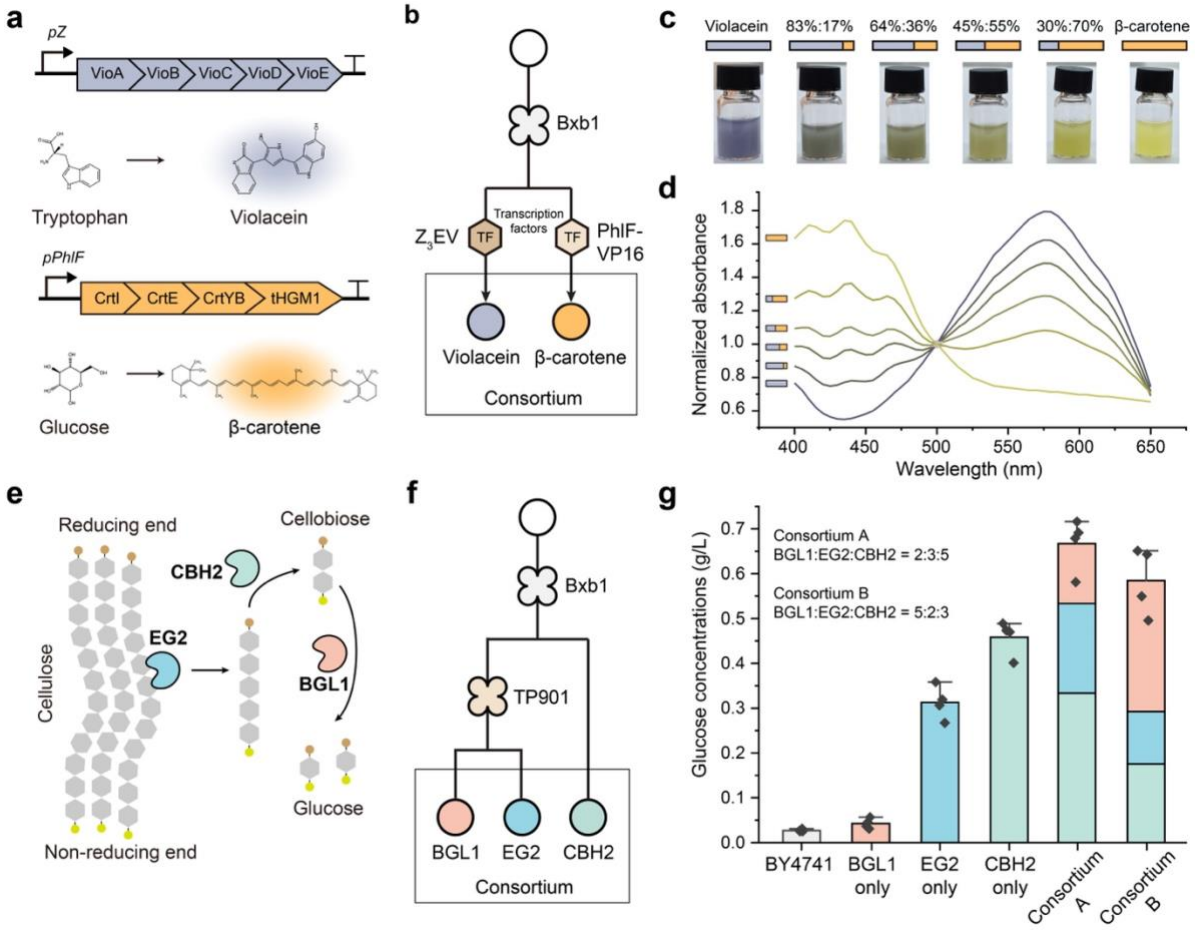

Fig. 5 | Engineering single-cell-controlled consortia for metabolic engineering. a, Diagram of enzymes involved in violacein (from tryptophan) and β-carotene (from glucose) synthesis. **b**, Founder cells differentiate into two progeny cell types producing either violacein or β-carotene enzymes, controlled by Z_3EV or PhIF-VP16 transcription factors, respectively. **c**, Photographs of yeast cultures producing violacein, β-carotene, or mixtures at varying ratios. **d**, Absorbance spectra of extracted pigments. **e**, Diagram of cellulase enzymes (CBH2, EG2, and BGL1) breaking down cellulose into glucose. **f**, Controlled generation of yeast consortia secreting three cellulases using branching devices. **g**, Comparison of reduced sugar production from cellulose by single-strain monocultures versus consortia (*n* = 4 independent experiments, mean ± SD).

Controllable self-organizing morphogenesis programmed by branching devices

The relative ratios and spatial arrangement of cell types, shaped by differentiation and cell-cell interactions, play a key role in the development of multicellular structures and morphogenesis[32-34]. We hypothesized that branching devices could be used to program multicellular morphologies beyond simple co-cultures created by manual mixing. To validate this, we incorporated yeast surface display systems (e.g., SED1 and GPI-anchored proteins)[35, 36], in combination with customized CAMs, such as antigen-antibody complexes, as branching device outputs.

As depicted in **Fig. 6a** and **Fig. 6b**, synthetic transcription factors Z_3EV and PhlF-VP16 were used to drive the expression of seven highly specific, orthogonal CAM pairs. Upon induction, this architecture enables engineered yeast to differentiate into two unique cell types, each displaying one of the CAM pairs, which facilitates the self-assembly of cell aggregates. To visualize these structures, green and red fluorescent proteins were co-expressed with the CAMs.

Microscopy confirmed the successful display of seven CAM pairs on yeast cell surfaces, with four pairs—Nb3-Ag3, Nb1-Ag1, Spytag-SpyCatcher, and Dockerin-Cohesin—showing strong aggregation-promoting properties (**Fig. 6c**). Flow cytometry further revealed elevated doublet ratios (exceeding 5%) for these four pairs, indicating a higher aggregation tendency in solution (**Fig. 6d, Fig. S75**). Using Nb3-Ag3 as a model, we investigated how altering cell-type ratios affected aggregate size. Adjusting the ratio of Nb3-to Ag3-expressing cells from 1:4 to 4:1 significantly influenced aggregate size, with more balanced ratios (e.g., 1:1) producing larger aggregates compared to imbalanced ones (e.g., 1:4 or 4:1) (**Fig. 6e-f, Fig. S76**). Additionally, sedimentation rates were higher for aggregates with balanced progeny ratios, indicating distinct physical properties (**Fig. 6g**).

To explore greater control over aggregate morphology, we studied the effects of cell-cell interactions on pattern formation. First, CAM branching devices were integrated into snowflake yeast, a strain that spontaneously forms multicellular aggregates[37] (**Fig. S77**). Combining the strain's inherent homophilic adhesion with engineered Nb3-Ag3 heterophilic adhesion (at ~1:1 ratios) led to the spontaneous separation of cell types within large aggregates, resembling weak phase separation[38] (**Fig. 6h**).

Switching to unicellular yeast, we removed heterophilic interactions and enhanced homophilic interactions by differentiating cells into two types: one co-displaying Nb3 and Ag3, and another co-displaying Nb1 and Ag1. This produced smaller, distinct aggregates with more pronounced phase separation (**Fig. 6i**). Finally, we engineered a three-member consortium using two orthogonal heterophilic interactions. Cells were differentiated into three types, displaying Ag1, Ag3, or Nb1+Nb3. The "double-sided tape" blue cells (displaying Nb1 and Nb3) adhered to both green (Ag1) and red (Ag3) cells, creating layered aggregates with blue cells separating the green and red populations. Interestingly, green and red cells also showed minor homophilic adhesion for unknown reasons (**Fig. 6j**).

In summary, we demonstrated that branching devices combined with CAMs, can generate complex, tunable morphologies in three dimensions. Most importantly, these structures were assembled autonomously through cell differentiation from one founder strain, without external intervention such as manual mixing. With advancements in CAM technology across species, branching devices hold great promise for tissue engineering and organoid development.

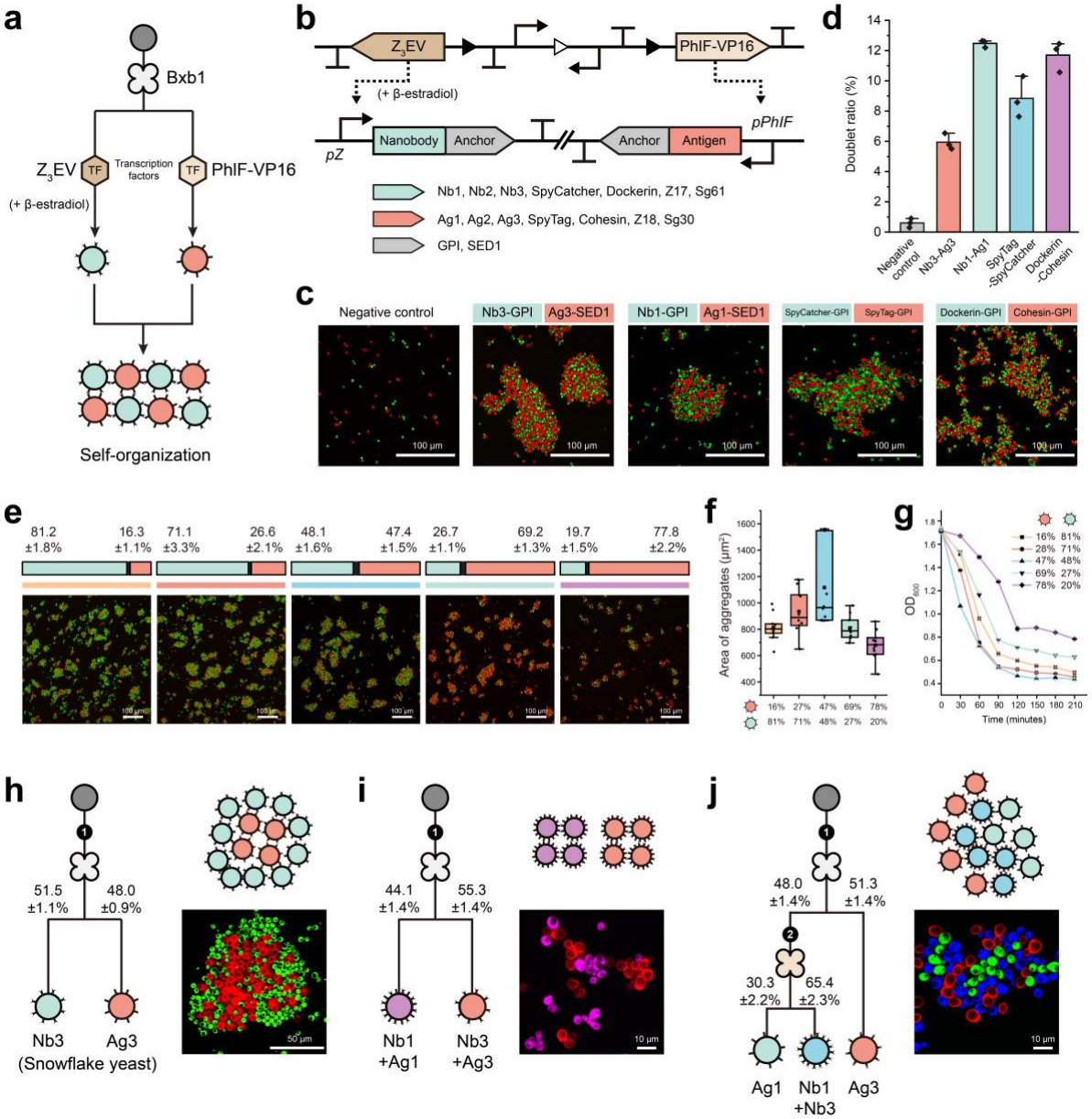

Fig. 6 | Engineering self-organized cellular morphogenesis via designed branching devices. a, Schematic of founder cells differentiating into two progeny types displaying specific cell adhesion molecule (CAM), driving cellular pattern formation. **b**, Genetic circuit design of branching devices generating CAM-displaying progeny cells. **c**, Fluorescence microscopy images of yeast consortia forming aggregates facilitated by CAM pairs (Nb3-Ag3, Nb1-Ag1, SpyTag-SpyCatcher, and Dockerin-Cohesin); negative control is the fluorescent BY4741 yeast cells lacking CAM-expression. **d**, Flow cytometry analysis showing elevated doublet ratios (> 5%) in CAM-expressing consortia, indicating increased cell aggregation. **e**, Fluorescence microscopy images of aggregates with varying ratios of Nb3- and Ag3-displaying cells (1:4 to 4:1). **f**, Comparison of aggregate sizes with different ratios of Nb3- and Ag3-displaying cells (n = 10 independent images, mean ± SD). **g**, Settling speeds of consortia with varying ratios of Nb3- and Ag3-displaying cells (n = 3 independent experiments, mean ± SD). **h**, Weak phase-separated cellular morphologies formed by snowflake yeast. **i**, Strong phase-separated cellular morphologies formed by Nb1-Ag1 or Nb3-Ag3 progeny cells. **j**, Layered morphology created by a progeny cell type adhering to two other cell types.

Discussion and Conclusion

Synthetic biology offers genetic tools with greater flexibility and predictability in controlling cell fate compared to natural systems, enabling the design of tailored cellular behaviors and more intricate functional networks that may not arise in nature. As a result, recent research has focused on using genetic circuits to emulate stem cells' asymmetric division and guide the differentiation of microbial communities or diverse eukaryotic tissues and organs[6-10, 39]. Despite these advances, a critical challenge remains: establishing a balanced quantitative relationship between functionally diverse progeny cell types within a consortium. To surmount this challenge, we have developed highly programmable and robust cell fate branching devices using recombinases. By exploiting the differential recombination efficiencies of these enzymes on user-defined DNA sequences, we have achieved precise quantitative control over binary cell fate branching and population composition. Integrating these orthogonal branching devices into various circuit topologies, we have crafted an expandable platform for parallel and series gene circuits, enabling precise ratio manipulation and effective management of progenitor and progeny diversity. Moreover, a data-driven computational model provides predictive insights, guiding the construction of cell differentiation programs that generate multiple cell types from a single founder strain in user-defined ratios.

To showcase the significance of ratio distribution, we applied branching device outputs to scenarios requiring specific consortia ratios, such as self-pigmentation, cellulose degradation, and autonomous cell assemblies. Previously, these applications relied on manually mixing of cell types for optimal performance[30, 38, 40, 41]. Our approach eliminates this manual step by condensing multiple genetic programs into a single founder strain capable of autonomous or conditional differentiation in response to external cues. Although our demonstrations featured two or three progeny cell types (**Fig. 5, Fig. 6**), the platform is highly modular and expandable. For example, in **Fig. 3f** and **Fig. 3g**, we showed that a single founder strain could differentiate into eight progeny types, each expressing a unique combination of three fluorescent proteins. By replacing these fluorescent proteins with transcription factors and using them to activate genetic programs controlled by 3-input AND gates[42, 43], one could create eight progeny cell types, each performing pathway-level tasks, as seen in **Fig. 5a**. The exponential scalability (2^n) of our parallel branching framework (**Fig. 3**), combined with advances in synthetic promoter design, suggests that systems with sixteen or more cell types are achievable.

Another promising direction involves engineering dependencies between progenitor and progeny cell types to create functionally and morphologically diverse cell assemblies[44, 45]. Inputs such as direct-contact signaling [46-48], or soluble communication[49], could replace the small-molecule inducers used in this study, enabling sequential, conditional differentiation for applications in organoids, tissue engineering, and metabolic engineering. Additionally, our framework can complement other artificial differentiation strategies utilizing asymmetric cell division[7, 9], or quorum sensing[50-52], to further enhance consortium stability. Notably, our system reserves a subpopulation of undifferentiated or partially differentiated progenitors due to incomplete recombination, which can be re-exposed to inducers to restore differentiation potential. This feature could be refined through programmed asymmetric division, as demonstrated in bacterial systems.

One challenge in our system is the sensitivity of ratio outputs to growth rate variations among differentiated cell types. Incorporating feedback mechanisms could stabilize ratios over longer timescales. Furthermore, when synthesizing proteins that reduce host fitness, traditional quorum-sensing-based devices could serve as fine-tuning mechanisms to lock specific ratios after the branching device establishes a coarse ratio. In conclusion, our branching device offers a modular, expandable, and rapid approach to programmable ratio-specific cell differentiation and pattern formation. Their universality across diverse organisms and independence from pre-established morphogen or quorum presence make them a versatile tool for applications ranging from metabolic engineering to tissue development, both in liquid and solid phases.

Methods

Bacterial strains and culture medium

All bacterial cloning experiments were performed using *E. coli* DH5α chemically competent cells (Tsingke). *E. coli* cultures were grown in lysogeny broth (LB) medium at 37 °C with shaking at 220 rpm. To maintain plasmids, LB medium was supplemented with antibiotics at the following concentrations: chloramphenicol at 34 μg/mL, carbenicillin at 100 μg/mL, kanamycin at 50 μg/mL, and spectinomycin at 100 μg/mL.

Plasmid construction

Plasmids were constructed using two modular cloning systems: the YTK system[53] (Dueber lab) and the MYT system[54] (Tom Ellis lab), both employing Golden Gate assembly. Assembly reactions were prepared as follows: 6.5 μL of DNA inserts, 1.0 μL of plasmid backbone, 1.0 μL of T4 DNA Ligase buffer (New England Biolabs), 0.5 μL of T4 DNA Ligase (New England Biolabs), 1.0 μL of a restriction enzyme, with the total volume adjusted to 10 μL. Restriction enzymes *Bsa* I (BsaI-HF v2, NEB) or *BsmB* I (*BsmB* I v2, NEB) were used. Thermocycling conditions consisted of 80 cycles of digestion (*Bsa* I at 37 °C or *BsmB* I at 42 °C for 5 minutes) and ligation (16 °C for 5 minutes), followed by digestion at 55 °C for 1 hour and heat inactivation at 80 °C for 10 minutes. Assembled plasmids were transformed into *E. coli* and cultured on LB agar with the appropriate antibiotic. Verification of plasmid DNA was performed via Sanger sequencing (Tsingke) and whole plasmid sequencing (KBSeq, Sangon Biotech). Genetic parts and protein sequences are listed in **Table. S4 and Table. S5,** while plasmid backbones and representative constructions are listed in **Table. S6 and Table. S7**.

DNA transformation into E. coli

DNA (1-10 μL) was mixed with 200 μL of freshly thawed competent *E. coli* and incubated on ice for 30 minutes. A 45-second heat shock at 42 °C was performed, followed by a 2-minute cooldown. The mixture was recovered in 500 μL antibiotic-free LB medium at 37 °C for 1 hour before plating on LB agar containing the relevant antibiotic.

Yeast strains and growth media

The *S. cerevisiae* strain BY4741 (MAT*a his3Δ1 leu2Δ0 met17Δ0 ura3Δ0 sed1*Δ) served as the default chassis for all experiments. Cultures were grown in yeast extract peptone dextrose (YPD) medium, consisting of 1.5% (w/v) yeast extract (Angel Yeast), 2.0% (w/v) peptone (Angel Yeast), and 2% (w/v) glucose (Sangon). Circuit induction and growth curve measurements used the YPD medium. For auxotrophy selection, SD minimal media (SD-Ura, SD-Leu, SD-His, and SD-Ura-Leu-His) containing 2% agar (Coolaber) were employed. Antibiotic selection used SD medium supplemented with 500

μg/mL hygromycin or 300 μg/mL zeocin, Snowflake yeast was created by deleting *ACE2* using a CRISPR-Cas9 system, as previously reported[37].

Yeast transformation

Plasmid DNA was pre-digested with the *Not* I enzyme in a reaction containing 1 μL of CutSmart buffer (NEB), 0.5 μL of NotI-HF enzyme (NEB), and 8.5 μL of plasmid DNA. Following digestion at 37 °C for 1 hour, 5 μL of the digested plasmid was mixed with boiled salmon sperm DNA (ssDNA) to a final volume of 10 μL. *S. cerevisiae* was cultured in YPD medium at 30 °C for 1-2 days. After culturing, 1 mL of the yeast solution was centrifuged at 5,000 rpm for 30 seconds at room temperature, and the cell pellet was washed three times with 1 mL of 0.1 M lithium acetate (LiOAc)[55]. After the final wash, the cells were resuspended in 50 μL of 0.1M LiOAc, and 2 μL was transferred to PCR tubes to serve as competent cells for each transformation. For the transformation, 10 μL plasmid-ssDNA was added to 2 μL of competent yeast cells. The mixture also included 22.4 μL of 50% PEG-3350 and 3.6 μL of 1 M LiOAc. After mixing well by gentle vortexing, the reaction was incubated at 42 °C and 30 °C for 40 minutes each. After the incubation, the yeast cells in the PCR tubes were centrifuged at 8,000 rpm for 20 seconds at room temperature. The supernatant was removed, and the cells were resuspended in 0.1 mL of sterile water. Transformed cells were plated on SD agar plates for auxotrophic or antibiotic selection.

Flow cytometry

On day 1, yeast strains were inoculated into 1 mL of YPD medium with inducers (1 mM aTc or 1 μM β-Estradiol) and cultured overnight in 2.2 mL deep-well plates at 30 °C with shaking at 800 rpm. On day 2, cells were diluted 1:50 in 200 μL of ddH_2O in a 96 flat-bottom plate for fluorescence using an Attune NxT Flow Cytometer (Thermo Scientific). Data from 10,000 cells per sample were analyzed using FlowJo software. For assessments of doublet ratios, yeast cells were diluted 1:5 in ddH_2O prior to measurement.

Growth curve measurements

Single yeast colonies were grown overnight in 1 mL of YPD medium at 30 °C with shaking at 800 rpm in a 2.2 mL 96 deep-well plate. The following day, cultures were diluted to an OD_{600} of approximately 0.06 in 200 μL of fresh YPD medium in a clear, flat-bottom 96-well microplate. OD_{600} readings were recorded every 5 minutes for 30 hours at 30 °C using a microplate reader (Biotek, SYNERGY H1), which included a 10-second shake before each measurement. The maximum growth rate during the exponential phase was calculated using the formula: $LN(OD_{600}(t + 6)/OD_{600}(t))/6$, where '*t*' is the time in hours.

Co-culture passaging

To evaluate the long-term stability of differentiated progeny cell consortia, yeast cells were cultured in predetermined proportions in 5 mL of YPD medium at 30 °C for one day. After this initial growth period, the proportions of each type of yeast within the consortia were analyzed using flow cytometry. For each subsequent round of growth, the yeast culture was diluted 1:1000 into 5 mL of fresh YPD medium and allowed to grow again for one day. This cycle of growth, dilution, and flow cytometry analysis was repeated for a total of seven rounds to monitor changes in the consortia composition over time.

NGS and analysis

Next-generation sequencing (NGS) via amplicon sequencing was performed on yeast cells encoding differentiation circuits. Yeast cultures were grown in 5 mL YPD and induced with either 1 mM aTc or 1 μM β-estradiol. Genomic DNA was extracted using a TIANamp Yeast DNA Kit (TIANGEN). A 300 bp DNA fragment undergoing recombinase-catalyzed rearrangement was amplified via PCR using genomic DNA as a template. The primers used for PCR were: forward primer (5'-cgacggcgatcacagacattaa-3') and reverse primer (5'-ctcacactgacgaatcatgt-3'). The amplified PCR products were purified and sent to Tsingke for NGS and data analysis.

Confocal fluorescence microscopy

For liquid-cultured yeast characterization, 5 μL of the yeast suspension was placed onto the center of a microscope slide. A clean 1 cm x 1 cm coverslip was gently placed over the droplet to ensure the even spreading of the solution. Once prepared, the sample was observed under a confocal fluorescence microscope (Nikon, AX). To characterize colonies grown on solid media, an SD medium containing 0.7% agar and appropriate inducers or antibiotics was prepared, allowed to cool, and solidified. A 2 μL aliquot of freshly cultured yeast solution (diluted 1:200 to an OD_{600} of approximately 0.06) was pipetted onto the agar surface. Plates were incubated at 30 °C for 3-5 days. After incubation, the colonies were imaged using the confocal fluorescence microscope.

Calculation of the area of yeast aggregates

Ten images of each engineered yeast aggregate depicted in **Fig. 5e** were captured using the confocal fluorescence microscope (Nikon, AX). The area of each yeast aggregate in the fluorescence images was quantified using ImageJ software. Areas smaller than 400 μm^2 were excluded from the analysis. The remaining data were compiled to create a graphical representation of yeast aggregate size distribution.

Sedimentation rate measurement

Yeast cells containing genetic circuits were cultured in 1.5 mL of induced YPD medium in 96 deep-well microplates at 30 °C and 800 rpm overnight. The yeast suspension was then adjusted to an OD_{600} of 1.7. One milliliter of yeast solution was transferred to a cuvette, and OD_{600} measurements were taken every 30 minutes for 210 minutes using a UV spectrophotometer. The collected data were analyzed to determine sedimentation rates.

Statistics and Reproducibility

All data was processed using Excel (Microsoft) and Origin (OriginLab) software. Error bars in the figures represent standard deviation, as specified in the figure legends. The number of replicates for each data set is also detailed in the figure legends, and all replicates have been included in the manuscript for comprehensive analysis.

Acknowledgments

This work was partially sponsored by the National Key R&D Program of China (2020YFA0908100 to C.Z), the National Science Fund for Distinguished Young Scholars (32125023 to C.Z.), the Shenzhen Science and Technology Program (ZDSYS20220606100606013 to C.Z.), the National Natural Science Foundation of China (32201105 to B.A.), the Shenzhen Medical Research Fund (A2403048 to B.A. and A2303072 to Q.Z.), and the China Postdoctoral Science Foundation (2023M733666 to Q.Z.). This work was also supported by the US Defense Advanced Research Projects Agency (DARPA) Engineered Living Materials award (W911NF-17-2-0077 to T.K.L.) and the US Department of Energy (DOE) (DE-FG02-02ER63445 to G.M.C.).

Author contributions

T.-C.T., C.Z., G.M.C., and B.A. conceptualized and directed the research. T.-C.T. built the branching device prototype in bacteria and yeast. B.A. designed and carried out most of the gene construction and flow cytometry experiments, with assistance from Q.Z., Y.L., K.G., Y.W., Q.L., and Y.W. Q.Z. contributed to the construction of snowflake yeast and pigment-producing strains. T.W. developed the mathematical model for progeny cell prediction. K.L. assisted with culturing HEK293 cells and characterizing the branching devices in mammalian cells. W.S. contributed to optimizing the yeast inducible systems. T.-C.T., T.K.L, G.M.C., B.A., and C.Z. contributed to funding acquisition. B.A., T.-C.T., C.Z., and G.M.C. wrote the manuscript, with input from all authors.

Competing interests

T-C.T. is a cofounder and equity holder of Anthology. T.K.L. is a cofounder of Senti Biosciences, Synlogic, Engine Biosciences, Tango Therapeutics, Corvium, BiomX, Eligo Biosciences, Bota.Bio, Avendesora and NE47Bio. T.K.L. also holds financial interests in nest.bio, Armata, IndieBio,

MedicusTek, Quark Biosciences, Personal Genomics, Thryve, Lexent Bio, March Therapeutics, Serotiny, Avendesora and Pulmobiotics. G.M.C disclosures can be found on the following webpage: https://arep.med.harvard.edu/gmc/tech.html. C.Z. is a cofounder and equity holder of Shenzhen PAM2L Biotechnologies Co., Ltd.

References

1. Fasching, L. et al. Early developmental asymmetries in cell lineage trees in living individuals. *Science* **371**, 1245-1248 (2021).
2. Junyent, S. et al. The first two blastomeres contribute unequally to the human embryo. *Cell* **187**, 2838-2854. e2817 (2024).
3. Tsokos, C.G. & Laub, M.T. Polarity and cell fate asymmetry in Caulobacter crescentus. *Current Opinion in Microbiology* **15**, 744-750 (2012).
4. Flores, E. & Herrero, A. Compartmentalized function through cell differentiation in filamentous cyanobacteria. *Nature Reviews Microbiology* **8**, 39-50 (2010).
5. Kong, W., Meldgin, D.R., Collins, J.J. & Lu, T. Designing microbial consortia with defined social interactions. *Nature Chemical Biology* **14**, 821-829 (2018).
6. Aditya, C., Bertaux, F., Batt, G. & Ruess, J. A light tunable differentiation system for the creation and control of consortia in yeast. *Nature Communications* **12**, 5829 (2021).
7. Molinari, S. et al. A synthetic system for asymmetric cell division in *Escherichia coli*. *Nature Chemical Biology* **15**, 917-924 (2019).
8. Dai, Y. et al. Programmable synthetic biomolecular condensates for cellular control. *Nature Chemical Biology* **19**, 518-528 (2023).
9. Mushnikov, N.V., Fomicheva, A., Gomelsky, M. & Bowman, G.R. Inducible asymmetric cell division and cell differentiation in a bacterium. *Nature Chemical Biology* **15**, 925-931 (2019).
10. Heng, Y.C., Kitano, S., Susanto, A.V., Foo, J.L. & Chang, M.W. Tunable cell differentiation via reprogrammed mating-type switching. *Nature Communications* **15**, 8163 (2024).
11. Zhu, J., Chu, P. & Fu, X. Unbalanced response to growth variations reshapes the cell fate decision landscape. *Nature Chemical Biology* **19**, 1097-1104 (2023).
12. Glass, D.S., Bren, A., Vaisbourd, E., Mayo, A. & Alon, U. A synthetic differentiation circuit in Escherichia coli for suppressing mutant takeover. *Cell* **187**, 931-944.e912 (2024).
13. Gardner, T.S., Cantor, C.R. & Collins, J.J. Construction of a genetic toggle switch in *Escherichia coli*. *Nature* **403**, 339-342 (2000).
14. Zhu, R., del Rio-Salgado, J.M., Garcia-Ojalvo, J. & Elowitz, M.B. Synthetic multistability in mammalian cells. *Science* **375**, eabg9765 (2022).
15. Siuti, P., Yazbek, J. & Lu, T.K. Synthetic circuits integrating logic and memory in living cells. *Nature Biotechnology* **31**, 448-452 (2013).
16. Weinberg, B.H. et al. Large-scale design of robust genetic circuits with multiple inputs and outputs for mammalian cells. *Nature Biotechnology* **35**, 453-462 (2017).
17. Bonnet, J., Yin, P., Ortiz, M.E., Subsoontorn, P. & Endy, D. Amplifying Genetic Logic Gates. *Science* **340**, 599-603 (2013).
18. Roquet, N., Soleimany, A.P., Ferris, A.C., Aaronson, S. & Lu, T.K. Synthetic recombinase-based state machines in living cells. *Science* **353**, aad8559 (2016).
19. Yang, L. et al. Permanent genetic memory with >1-byte capacity. *Nature Methods* **11**, 1261-1266 (2014).
20. Guiziou, S., Mayonove, P. & Bonnet, J. Hierarchical composition of reliable recombinase logic devices. *Nature Communications* **10**, 456 (2019).
21. Zhang, Q., Azarin, S.M. & Sarkar, C.A. Model-guided engineering of DNA sequences with predictable site-specific recombination rates. *Nature Communications* **13**, 4152 (2022).
22. Keenholtz, R.A., Grindley, N.D.F., Hatfull, G.F. & Marko, J.F. Crossover-site sequence and DNA torsional stress control strand interchanges by the Bxb1 site-specific serine recombinase. *Nucleic Acids Research* **44**, 8921-8932 (2016).
23. Jusiak, B. et al. Comparison of Integrases Identifies Bxb1-GA Mutant as the Most Efficient Site-Specific Integrase System in Mammalian Cells. *ACS Synthetic Biology* **8**, 16-24 (2019).
24. Durrant, M.G. et al. Systematic discovery of recombinases for efficient integration of large DNA sequences into the human genome. *Nature Biotechnology* **41**, 488-499 (2023).
25. Xu, Z. & Brown, W.R.A. Comparison and optimization of ten phage encoded serine integrases for genome engineering in Saccharomyces cerevisiae. *BMC Biotechnology* **16**, 13 (2016).
26. Rantasalo, A., Kuivanen, J., Penttilä, M., Jäntti, J. & Mojzita, D. Synthetic Toolkit for Complex Genetic Circuit Engineering in Saccharomyces cerevisiae. *ACS Synthetic Biology* **7**, 1573-1587 (2018).
27. Turing, A.M. The chemical basis of morphogenesis. *Philosophical Transactions of the Royal Society of London. Series B, Biological Sciences* **237**, 37-72 (1952).
28. Mitchell, L.A. et al. Versatile genetic assembly system (VEGAS) to assemble pathways for

expression in S. cerevisiae. *Nucleic Acids Research* **43**, 6620-6630 (2015).
29. Walker, K.T. et al. Self-pigmenting textiles grown from cellulose-producing bacteria with engineered tyrosinase expression. *Nature Biotechnology*, https://doi.org/10.1038/s41587-41024-02194-41583 (2024).
30. Lee, C.-R. et al. Co-fermentation using Recombinant Saccharomyces cerevisiae Yeast Strains Hyper-secreting Different Cellulases for the Production of Cellulosic Bioethanol. *Scientific Reports* **7**, 4428 (2017).
31. Wood, I.P. et al. Rapid quantification of reducing sugars in biomass hydrolysates: Improving the speed and precision of the dinitrosalicylic acid assay. *Biomass and Bioenergy* **44**, 117-121 (2012).
32. Chao, G. et al. helixCAM: A platform for programmable cellular assembly in bacteria and human cells. *Cell* **185**, 3551-3567.e3539 (2022).
33. Toda, S., Blauch, L.R., Tang, S.K.Y., Morsut, L. & Lim, W.A. Programming self-organizing multicellular structures with synthetic cell-cell signaling. *Science* **361**, 156-162 (2018).
34. Toda, S. et al. Engineering synthetic morphogen systems that can program multicellular patterning. *Science* **370**, 327-331 (2020).
35. Li, Y., Wang, X., Zhou, N.-Y. & Ding, J. Yeast surface display technology: Mechanisms, applications, and perspectives. *Biotechnology Advances* **76**, 108422 (2024).
36. McMahon, C. et al. Yeast surface display platform for rapid discovery of conformationally selective nanobodies. *Nature Structural & Molecular Biology* **25**, 289-296 (2018).
37. Bozdag, G.O. et al. De novo evolution of macroscopic multicellularity. *Nature* **617**, 747-754 (2023).
38. Glass, D.S. & Riedel-Kruse, I.H. A Synthetic Bacterial Cell-Cell Adhesion Toolbox for Programming Multicellular Morphologies and Patterns. *Cell* **174**, 649-658.e616 (2018).
39. Wauford, N. et al. Synthetic symmetry breaking and programmable multicellular structure formation. *Cell Systems* **14**, 806 - 818 (2023).
40. Peng, H. et al. A molecular toolkit of cross-feeding strains for engineering synthetic yeast communities. *Nature Microbiology* **9**, 848-863 (2024).
41. Tordoff, J. et al. Incomplete Cell Sorting Creates Engineerable Structures with Long-Term Stability. *Cell Reports Physical Science* **2**, 100305 (2021).
42. Shis, D.L., Hussain, F., Meinhardt, S., Swint-Kruse, L. & Bennett, M.R. Modular, Multi-Input Transcriptional Logic Gating with Orthogonal LacI/GalR Family Chimeras. *ACS Synthetic Biology* **3**, 645-651 (2014).
43. Chen, Y. et al. Tuning the dynamic range of bacterial promoters regulated by ligand-inducible transcription factors. *Nature Communications* **9**, 64 (2018).
44. Weatherbee, B.A.T. et al. Pluripotent stem cell-derived model of the post-implantation human embryo. *Nature* **622**, 584-593 (2023).
45. Lim, W.A. The emerging era of cell engineering: Harnessing the modularity of cells to program complex biological function. *Science* **378**, 848-852 (2022).
46. Meng, F., Shaw, W.M., Kam, Y.K.K. & Ellis, T. Engineered yeast multicellularity via synthetic cell-cell adhesion and direct-contact signalling. *BioRxiv*, 2024.2006.2023.600301 (2024).
47. Morsut, L. et al. Engineering Customized Cell Sensing and Response Behaviors Using Synthetic Notch Receptors. *Cell* **164**, 780-791 (2016).
48. Zhang, X. et al. Post-Transcriptional Modular Synthetic Receptors. *BioRxiv*, 2024.2005.2003.592453 (2024).
49. Piraner, D.I. et al. Engineered receptors for soluble cellular communication and disease sensing. *Nature* (2024).
50. Alnahhas, R.N. et al. Majority sensing in synthetic microbial consortia. *Nature Communications* **11**, 3659 (2020).
51. Daneshpour, H., van den Bersselaar, P., Chao, C.-H., Fazzio, T.G. & Youk, H. Macroscopic quorum sensing sustains differentiating embryonic stem cells. *Nature Chemical Biology* **19**, 596-606 (2023).
52. Moreno-Gámez, S., Hochberg, M.E. & van Doorn, G.S. Quorum sensing as a mechanism to harness the wisdom of the crowds. *Nature Communications* **14**, 3415 (2023).
53. Lee, M.E., DeLoache, W.C., Cervantes, B. & Dueber, J.E. A Highly Characterized Yeast Toolkit for Modular, Multipart Assembly. *ACS Synthetic Biology* **4**, 975-986 (2015).
54. Shaw, W.M., Khalil, A.S. & Ellis, T. A Multiplex MoClo Toolkit for Extensive and Flexible Engineering of *Saccharomyces cerevisiae*. *ACS Synthetic Biology* **12**, 3393-3405 (2023).
55. Gietz, R.D. & Schiestl, R.H. High-efficiency yeast transformation using the LiAc/SS carrier

DNA/PEG method. *Nature Protocols* **2**, 31-34 (2007).